

mixed state described by a density matrix ρ . The setup efficiency is thus characterized by a fidelity $F = \langle \Psi_{\text{triplet}} | \rho | \Psi_{\text{triplet}} \rangle$. If the detection stages (Fig. 2, B and C) were perfect, F would be equal to the sum $P_{\parallel}/2 + V_{\perp}$ (14). However, the value of this quantity, 0.43, is affected by known detection errors and F is actually larger. Trivial imperfections can occur at three different stages: the mapping of the cavity state onto A_3 ; the classical microwave pulses $R_2^{(i)}$, $R_1^{(i)}$, and $R_3^{(i)}$; and the energy state-selective atom counting. We have determined these errors independently by additional single-atom experiments. Taking them into account, we determine a fidelity $F = 0.54 \pm 0.03$. The three kinds of errors listed above account respectively for corrections of 0.03, 0.05, and 0.03 to the raw 0.43 value. The fact that F is larger than 0.5 ensures that genuine three-particle entanglement is prepared here (14).

The combined results of experiments I and II demonstrate the step-by-step engineered entanglement of three qubits, manipulated and addressed individually. By adjusting the various pulses, the experiment could be programmed to prepare a tailored three-particle state. One drawback of our apparatus is that atomic coherences cannot exit the cavity-ring structure. There are now good prospects for realizing a better cavity without any ring, relaxing the tight timing constraints and improving the fidelity. At present, the main limitation is that circular atoms are prepared with Poisson statistics with a low mean value, requiring long data acquisition times. However, it is possible to implement preparation techniques for circular states that generate exactly one atom on demand. For instance, the fluorescence from a weak atomic beam can be used to image a single atom and excite it deterministically to the circular state in a fully adiabatic process. With these improvements, the techniques described here could be extended to more complex systems.

Tests of quantum nonlocality on many-particle generalizations of the GHZ triplet (29) are particularly appealing. These states are generated by a simple iteration of the present scheme (18, 19). After having prepared the A_1 - C pair in the state described by Eq. 1, one sends a stream of atoms A_2 - A_3 -...- A_n all prepared in $(|i\rangle + |g\rangle)/\sqrt{2}$ and undergoing, if in g , a 2π Rabi rotation in a single-photon field. Because this rotation does not change the photon number, the zero- and one-photon parts of the A_1 - C system become correlated to an A_2 - A_3 -...- A_n state, with all $n - 1$ atoms in $(|i\rangle + |g\rangle)/\sqrt{2}$ for the zero-photon and in $(|i\rangle - |g\rangle)/\sqrt{2}$ for the one-photon part, preparing the entangled state

$$|\Psi\rangle = \frac{1}{\sqrt{2}} (|+1, +2, \dots, +n\rangle - |-1, -2, \dots, -n\rangle) \quad (8)$$

Teleportation experiments operating on mas-

sive particles instead of photons are also within reach with an improved version of the setup (30).

References and Notes

1. C. H. Bennett and D. P. DiVincenzo, *Nature* **404**, 247 (2000).
2. A. Einstein, B. Podolsky, N. Rosen, *Phys. Rev.* **47**, 777 (1935).
3. A. Zeilinger, *Rev. Mod. Phys.* **71**, S288 (1998).
4. C. H. Bennett et al., *Phys. Rev. Lett.* **70**, 1895 (1993).
5. J.-W. Pan et al., *Nature* **390**, 575 (1998).
6. D. Boschi, S. Branca, F. De Martini, L. Hardy, S. Popescu, *Phys. Rev. Lett.* **80**, 1121 (1998).
7. A. Furusawa et al., *Science* **282**, 706 (1998).
8. C. H. Bennett, G. Brassard, A. Ekert, *Sci. Am.* (October 1992), p. 50.
9. J. G. Rarity, P. C. M. Owens, P. R. Tapster, *J. Mod. Opt.* **41**, 2435 (1994).
10. J. W. Pan, D. Bouwmeester, M. Daniell, H. Weinfurter, A. Zeilinger, *Nature* **403**, 515 (2000).
11. N. A. Gershenfeld and I. L. Chuang, *Science* **275**, 350 (1997).
12. S. L. Braunstein et al., *Phys. Rev. Lett.* **83**, 1054 (1999).
13. Q. A. Turchette et al., *Phys. Rev. Lett.* **81**, 3631 (1998).
14. C. A. Sackett et al., *Nature* **404**, 256 (2000).
15. E. Hagley et al., *Phys. Rev. Lett.* **79**, 1 (1997).
16. P. Domokos, J. M. Raimond, M. Brune, S. Haroche, *Phys. Rev. A* **52**, 3554 (1995).
17. A three-atom-cavity experiment was recently reported [B. T. H. Varcoe, S. Brattke, M. Weidinger, H. Walther, *Nature* **403**, 743 (2000)]. It exhibited atomic energy correlations but did not detect entanglement.
18. S. Haroche et al., in *Laser Spectroscopy 14*, R. Blatt, J. Eschner, D. Leibfried, F. Schmidt-Kaler, Eds. (World Scientific, New York, 1999), pp. 140–149.

19. S. B. Zheng, *J. Opt. B* **1**, 534 (1999).
20. M. Brune et al., *Phys. Rev. Lett.* **76**, 1800 (1996).
21. X. Maître et al., *Phys. Rev. Lett.* **79**, 769 (1997).
22. A. Rauschenbeutel et al., *Phys. Rev. Lett.* **83**, 5166 (1999).
23. G. Noguez et al., *Nature* **400**, 239 (1999).
24. P. Nussenzveig et al., *Phys. Rev. A* **48**, 3991 (1993).
25. D. M. Greenberger, M. A. Horne, A. Zeilinger, *Am. J. Phys.* **58**, 1131 (1990).
26. S. Haroche, *Ann. N.Y. Acad. Sci.* **755**, 73 (1995).
27. B. T. H. Varcoe, S. Brattke, B.-G. Englert, H. Walther, in *Laser Spectroscopy 14*, R. Blatt, J. Eschner, D. Leibfried, F. Schmidt-Kaler, Eds. (World Scientific, New York, 1999), pp. 130–139.
28. Because the experiment involves three levels for each atom, there are 27 detection channels in all. We only give the channels corresponding to the relevant transitions for each atom: $e \rightarrow g$ for A_1 and A_3 ; $g \rightarrow i$ for A_2 . The other channels are weakly populated by spurious effects such as spontaneous emission outside C , residual thermal photons, influence of the $R_2^{(i)}$ or P_2 pulses on the other atoms, and absorption of the cavity field by A_2 as a result of imperfect 2π Rabi rotation. The total contribution of these transfer processes is less than 15%.
29. N. D. Mermin, *Phys. Rev. Lett.* **65**, 1838 (1990).
30. L. Davidovich, N. Zagury, M. Brune, J. M. Raimond, S. Haroche, *Phys. Rev. A* **50**, R895 (1994).
31. Laboratoire Kastler Brossel is a Unité Mixte de Recherche, Ecole Normale Supérieure, Université Pierre et Marie Curie et CNRS (UMR8552). Supported in part by the European Community and Japan Science and Technology Corporation (International Cooperative Research Project, Quantum Entanglement project). We thank P. Goy and M. Gross for help with the microwave technology.

29 March 2000; accepted 20 April 2000

Assessment of Oceanic Productivity with the Triple-Isotope Composition of Dissolved Oxygen

Boaz Luz* and Eugeni Barkan

Plant production in the sea is a primary mechanism of global oxygen formation and carbon fixation. For this reason, and also because the ocean is a major sink for fossil fuel carbon dioxide, much attention has been given to estimating marine primary production. Here, we describe an approach for estimating production of photosynthetic oxygen, based on the isotopic composition of dissolved oxygen of seawater. This method allows the estimation of integrated oceanic productivity on a time scale of weeks.

Our knowledge of the rate of marine photosynthetic production is based primarily on bottle incubation experiments (1). These experiments provide local instantaneous primary production rates, which often miss the effects of significant blooms because of the heterogeneous distribution of plankton in time and space. A broader view of marine primary production can be obtained from satellite remote sensing (2). However, values de-

rived by this method depend on the quality of calibration data obtained by actual productivity measurements in the ocean and cannot be better than the accuracy of this information. Here, we present a way to estimate marine production that alleviates the inherent problems of incubation methods. In this approach, gross production, integrated on spatial and temporal scales, is estimated from the difference between the triple isotope (^{16}O , ^{17}O , and ^{18}O) composition of atmospheric and dissolved O_2 and the rate of air-sea O_2 exchange.

Most terrestrial processes fractionate O isotopes in a mass-dependent way, such that ^{17}O

The Institute of Earth Sciences, The Hebrew University of Jerusalem, Jerusalem 91904, Israel.

*To whom correspondence should be addressed.

REPORTS

enrichment is about half of ¹⁸O enrichment relative to ¹⁶O. As a result, δ¹⁷O and δ¹⁸O in terrestrial materials plot along a line with a mass-dependent slope of about 0.52. This δ¹⁷O/δ¹⁸O slope represents an average of slightly different slopes of various mass-dependent processes (3). For example, the δ¹⁷O and δ¹⁸O of O₂ produced by photosynthesis and fractionated by respiration vary along a line with a slope of 0.521 (4), but fractionation of O isotopes in the formation of meteoric precipitation occurs with a slightly steeper slope, 0.534 (5). In contrast to these mass-dependent processes, ultraviolet (UV)-induced interactions among O₂, O₃, and CO₂ in the stratosphere cause mass-independent fractionation (6) with equal lowering of δ¹⁷O and δ¹⁸O in atmospheric O₂ (4). Therefore, for a given δ¹⁸O of O₂ produced solely by biological production and consumption, there is an excess of ¹⁷O in comparison to air O₂. This ¹⁷O excess (Δ¹⁷O) with respect to air O₂ is defined as

$$\Delta^{17}\text{O} = 1000(\delta^{17}\text{O} - 0.521\delta^{18}\text{O}) \quad (1)$$

By definition, δ¹⁸O, δ¹⁷O, and Δ¹⁷O of air O₂ equal zero (7).

The Δ¹⁷O value of dissolved O₂ (Δ_{diss}) depends on the rate of air-water gas exchange, which tends to bring Δ_{diss} to an equilibrium value with air, and the rate of in situ production of biological O₂, which tends to increase Δ_{diss} to a maximum value of pure biological O₂ (Δ_{max}). In natural aquatic systems, Δ_{diss} varies

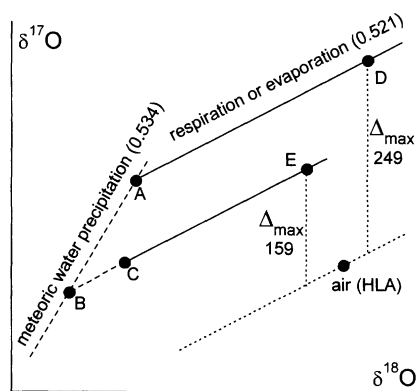


Fig. 1. Schematic plot (not to scale) of δ¹⁷O, δ¹⁸O, and Δ_{max} variations among seawater, meteoric water, air O₂, and biological O₂. Graphically, Δ¹⁷O is the vertical distance from the line with 0.521 slope going through the point representing the HLA air standard. In pure biological O₂, Δ¹⁷O = Δ_{max}. Point A represents ocean water and point D represents biological O₂ (Δ_{max} = 249 per meg) produced from point A and fractionated by respiration along a line with δ¹⁷O/δ¹⁸O slope of 0.521. Point B represents meteoric water fractionated along the line with δ¹⁷O/δ¹⁸O slope of 0.534. Subsequent evaporation fractionated this water along a line with δ¹⁷O/δ¹⁸O slope of 0.521 to form the water of the Sea of Galilee (point C). Point E represents biological O₂ (Δ_{max} = 159 per meg) produced from C and fractionated by respiration.

between these two extremes, and its value depends on the ratio of the rates of gross primary production and air-sea O₂ exchange. Thus, gross production can be calculated from Δ_{diss} if the rate of air-sea gas exchange is known.

Isotopic analysis of water seems to be a straightforward way to determine Δ_{max} variations. However, the error of individual Δ¹⁷O measurements of H₂O is relatively large [±75 per meg (1000 per meg = 1‰) (5)], and the value of Δ¹⁷O of H₂O is very sensitive to the slope used in Eq. 1 for its calculation (8). For these reasons, we have determined Δ_{max} in closed system experiments in which O₂ was produced and consumed in the absence of UV radiation.

In a previous study, Δ_{max} was determined from the Δ¹⁷O of O₂ produced by *Philodendron* (a higher plant) in terrariums containing water from the Sea of Galilee and from the Dan River (4). This river is a major water source of the Sea of Galilee, but the latter is enriched in ¹⁸O by about 5‰ due to evaporative loss of water vapor. The Δ_{max} values were 155 ± 15 and 156 ± 7 per meg for the Sea of Galilee and the Dan River, respectively. This shows that evaporation from the lake surface does not affect Δ_{max}, because it causes δ¹⁷O and δ¹⁸O to increase along a slope of 0.521 (Fig. 1).

As discussed below, accurate Δ_{max} values are critical for estimating true aquatic productivity. Therefore, we conducted additional experiments with marine and freshwater organisms (9). The Δ_{max} of O₂ produced from fresh water by *Peridinium* (a major producer in the Sea of Galilee) was 159 ± 10 per meg, very close to the value determined for the same water by a completely different plant, *Philodendron* (10). The Δ_{max} values of O₂ produced from seawater by marine organisms—

planktonic algae (*Nannochloropsis*) and corals (*Acropora*) with their symbiotic algae—were 244 ± 20 and 252 ± 5 per meg, respectively. The different Δ_{max} values of seawater and water from the Sea of Galilee are expected because meteoric water has different δ¹⁷O/δ¹⁸O slope than that of biological uptake (Fig. 1). It should be emphasized that our experiments clearly show that the values of Δ_{max} are independent of the type of organisms producing and consuming O₂. Finally, isotopic variations of seawater from different parts of the ocean are small (11), and thus an average Δ_{max} value of 249 ± 15 per meg should be representative of the entire ocean.

In order to derive quantitative estimates of gross production, we consider a simple model in which the aquatic mixed layer, in contact with air, is in a steady state with respect to O₂ concentration and Δ_{diss} and vertical mixing with deeper water is neglected. In the absence of biological activity, Δ_{diss} is expected to be close to Δ¹⁷O of air O₂, and thus approximately zero. However, in the case of air-water equilibration, we determined equilibrium Δ_{diss} (Δ_{eq}) of 16 per meg (12). This small deviation of Δ_{eq} from zero suggests that the δ¹⁷O/δ¹⁸O slopes in invasion and evasion of O₂ are slightly different than 0.521. We assume that the positive Δ_{eq} is the result of fractionation during O₂ invasion alone (12). Thus, the Δ¹⁷O balance in the mixed layer is given by

$$I\Delta_{\text{eq}} + GP\Delta_{\text{max}} = E\Delta_{\text{diss}} + R\Delta_{\text{diss}} \quad (2)$$

where *I* and *E* are the rates of atmospheric O₂ invasion and evasion, respectively, *GP* is O₂ gross production, and *R* is total oxygen consumption. The difference between evasion and invasion fluxes is the net biological O₂ flux, and in our simplified case it equals *P* - *R*. Noting that *I* = *K**C*_o [where *K* is the coefficient of gas exchange (piston velocity) and *C*_o is equilibrium O₂ concentration], Eq. 2 can be rewritten as

$$GP = KC_o(\Delta_{\text{diss}} - \Delta_{\text{eq}})/(\Delta_{\text{max}} - \Delta_{\text{diss}}) \quad (3)$$

We have applied the new method in the highly productive Sea of Galilee and in the

Table 1. Estimates of gross production (*GP*, mmol m⁻² day⁻¹) in the Sea of Galilee obtained from the Δ¹⁷O method [*GP*(Δ¹⁷)] and from bottle incubations with H₂¹⁸O spike [*GP*(H₂¹⁸O)]. The *GP*(H₂¹⁸O) values represent depth integration over the entire euphotic zone. The Δ_{diss} values are in per meg units. For applying Eq. 3, we used Δ_{max} = 159 per meg; values of O₂ solubility were taken from (19); piston velocities were calculated according to (13) from daily wind speeds and then averaged over 1 week. The error propagation for *GP*(Δ¹⁷) reflects uncertainties in Δ_{max}, Δ_{eq}, and Δ_{diss}.

Date	Δ _{diss}	<i>GP</i> (Δ ¹⁷)	<i>GP</i> (H ₂ ¹⁸ O)
15 Feb. 1998	106	352 ± 54	287 ± 27
15 Mar. 1998	131	844 ± 213	1007 ± 90
5 Apr. 1998	130	801 ± 278	916 ± 86
3 May 1998	143	1905 ± 390	1938 ± 190
14 Jun. 1998	133	1225 ± 435	1021 ± 102
4 Aug. 1998	98	304 ± 69	379 ± 35
15 Nov. 1998	98	194 ± 27	184 ± 16
14 Dec. 1998	94	204 ± 28	214 ± 17
11 Jan. 1999	77	120 ± 18	112 ± 8
21 Feb. 1999	107	307 ± 44	357 ± 33

Table 2. Estimates of gross production (*GP*, mmol m⁻² day⁻¹) in the BATS Station obtained from the Δ¹⁷O method [*GP*(Δ¹⁷)]. The Δ_{diss} values are in per meg units. For applying Eq. 3, we used Δ_{max} = 249 per meg; values of O₂ solubility (*C*_o, mmol m⁻³) were taken from (19); piston velocities (*K*, m day⁻¹) were calculated from climatological wind speeds (20). Error propagation as in Table 1.

Date	<i>C</i> _o	<i>K</i>	Δ _{diss}	<i>GP</i> (Δ ¹⁷)
7 Jul. 1998	203.6	2.7	30	35 ± 12
7 Sep. 1998	199.7	1.8	46	53 ± 13
7 Nov. 1998	213.6	2.7	47	87 ± 21
24 Jan. 1999	222.0	4.4	43	130 ± 34
23 Mar. 1999	230.3	4.4	33	82 ± 24
15 Jul. 1999	203.5	2.7	30	35 ± 12

BATS (Bermuda Atlantic Time-series Study) Station located in the low-productivity region of the Atlantic Ocean. The Sea of Galilee is a simple case where the entire photic zone, and thus all gross production, is confined to the mixed layer of about 10 m depth. The spatial distribution of O_2 and Δ_{diss} in the mixed layer is uniform and the residence time of O_2 is about 5 days. The results for the Sea of Galilee (Table 1) show the expected seasonal cycle with higher productivity in spring and summer, and are in excellent agreement with the estimates obtained from bottle incubations with $H_2^{18}O$ spike (1). We notice that the uncertainty in $GP(\Delta^{17}O)$ sharply increases when Δ_{diss} values in the lake approach the biological limit of Δ_{max} . With the exception of this extreme situation, errors in GP due to inaccuracies in Δ_{max} , Δ_{eq} , and Δ_{diss} are on the order of about 30%, and are smaller than errors associated with uncertainties in piston velocities (13). Therefore, improvement in estimation of GP is likely to come mainly from better knowledge of gas exchange rates, which can be gained by deliberate tracer experiments (14).

In the BATS Station, the situation is more complex because photosynthesis takes place in both the mixed layer as well as in the underlying thermocline. In Fig. 2, we show the depth distribution of Δ_{diss} , temperature, and $\delta O_2/Ar$ (deviation of the O_2/Ar ratio of dissolved gases from the O_2/Ar ratio in air). Variations in $\delta O_2/Ar$ reflect production and consumption of O_2 independent of physical processes affecting O_2 concentration (15). In July, the $\delta O_2/Ar$ had a maximum at 40 m, corresponding to the typical subsurface oxygen maximum of the summer thermocline. As has been noted by Jenkins and co-workers (16), this originates from the seasonal net accumulation of photosynthetic O_2 . The Δ_{diss} curve also has a maximum in the summer thermocline, indicating in situ gross O_2 production. The maximum Δ_{diss} is analogous to the subsurface $\delta O_2/Ar$ maximum—both maxi-

ma are formed from attenuation of vertical mixing caused by density stratification in the thermocline. In November, the mixed layer was deeper due to cooling and extended down to 60 m. As in July, a Δ_{diss} maximum was present in the thermocline, but in contrast, there was no $\delta O_2/Ar$ maximum. The pronounced Δ_{diss} maximum indicates continued in situ O_2 production, but the relatively low values of $\delta O_2/Ar$ show that O_2 uptake was greater than its generation. Finally, with further cooling in March the mixed layer extended to a depth below the photic zone, and in the absence of photosynthesis in the thermocline, the Δ_{diss} maximum disappeared.

Initial estimates of GP are given in Table 2. These estimates are time-integrated rates representing production in the mixed layer as well as gains and losses due to vertical mixing with the underlying thermocline. The residence time of O_2 in the mixed layer is about 2 weeks, and thus effects of short events of high production are expected to average out by the lower background of the entire mixed layer. When the mixed layer is shallow and the thermocline is situated in the photic zone, the calculated GP rates should be considered as minimum values, because some of the production takes place below the mixed layer, as is evident in the Δ_{diss} maximum in the thermocline (Fig. 2). This is probably an ocean-wide phenomenon, because in addition to BATS, we have observed Δ_{diss} maxima in the thermocline in the Red Sea and in the equatorial Indian Ocean (17). Conversely, when deep mixing takes place in winter, the calculated GP should be considered as maximum because some of the dissolved O_2 with high Δ_{diss} in the thermocline is incorporated into the mixed layer. Over an annual cycle, the winter excess should compensate for the summer deficit, and an annual integration of the calculated GP is expected to reliably reflect the true integrated production in a given area. Lateral transport has been neglected in this simple one-dimensional description, but it can be represent-

ed in future studies by applying general circulation models.

The trend of seasonal variations of GP in BATS, with a late winter maximum and a summer minimum (Table 2), is similar to the general pattern of productivity observed in other studies (18). Annual integrated production was calculated from the data in Table 2 as 28 mol $O_2 m^{-2} year^{-1}$. The integrated annual C fixation for the period 1988–94 estimated from ^{14}C incubation experiments ranged from about 9 to 14 mol C $m^{-2} year^{-1}$ (18). Thus, annual O_2 gross production is about two to three times the estimated annual C fixation. Similar ratios between O_2 gross production and C fixation have been reported in studies based on direct comparisons of ^{14}C and $H_2^{18}O$ incubation experiments (1), demonstrating the capability of the method we report to derive reliable estimates of gross production. Although more studies are needed in order to gain a comprehensive global picture, such a view is now more attainable.

References and Notes

1. M. L. Bender et al., *Limnol. Oceanogr.* **32**, 1085 (1987); M. L. Bender, H. Ducklow, J. Kiddon, J. Marra, J. Martin, *Deep-Sea Res. I* **39**, 1707 (1992); R. T. Barber et al., *Deep-Sea Res. II* **43**, 933 (1996); P. J. L. Williams, *Nature* **394**, 55 (1998); J. J. McCarthy, C. Garside, J. L. Nevins, *Deep-Sea Res. II* **46**, 1623 (1999).
2. M. J. Berghrenfeld and P. G. Falkowski, *Limnol. Oceanogr.* **42**, 1 (1997).
3. R. N. Clayton, L. Grossman, T. K. Mayeda, *Science* **182**, 485 (1973); Y. Matsuhisa, J. R. Goldsmith, R. N. Clayton, *Geochim. Cosmochim. Acta* **42**, 173 (1978).
4. B. Luz, E. Barkan, M. L. Bender, M. H. Thiemeis, K. A. Boering, *Nature* **400**, 547 (1999).
5. W. J. Li and H. A. J. Meijer [*Isotopes Environ. Health Stud.* **34**, 349 (1998)] determined the isotopic composition of meteoric water with respect to seawater. The $\delta^{17}O/\delta^{18}O$ slope of 0.534 is based on their $\delta^{17}O$ and $\delta^{18}O$ data expressed with respect to air O_2 .
6. M. H. Thiemeis, T. L. Jackson, C. A. M. Brenninkmeijer, *Geophys. Res. Lett.* **22**, 225 (1995).
7. Ratios of $^{18}O/^{16}O$ and $^{17}O/^{16}O$ are reported as $\delta^{\circ}O$ (‰) = $1000[(^{18}O/^{16}O_{sample})/(^{18}O/^{16}O_{HLA}) - 1]$ where $^{\circ}O$ denotes ^{17}O or ^{18}O and HLA (Holy Land Air) is an air O_2 standard. The $\Delta^{17}O$ value is given in per meg units (1000 per meg = 1‰). The average total analytical error in $\Delta^{17}O$ of dissolved O_2 , based on duplicate measurements, is 3 per meg. Dissolved gases were extracted from water according to S. Emerson, P. D. Quay, C. Stump, D. Wilbur, and R. Schudlich [*J. Geophys. Res.* **100**, 15873 (1995)], and processed to yield an O_2 -Ar mixture for measurement on a Finnigan Delta-Plus mass spectrometer.
8. In the case where Eq. 1 is applied with $\delta^{18}O = -20‰$, $\delta^{17}O = -10.4‰$, a 0.521 slope yields $\Delta^{17}O$ of 20 per meg, but a 0.525 slope yields $\Delta^{17}O$ of 100 per meg. In contrast, $\delta^{17}O$ and $\delta^{18}O$ of O_2 produced by photosynthesis and fractionated by respiration are close to the zero value of the HLA standard, and the value of Δ_{diss} is not sensitive to the slope term in Eq. 1.
9. The experiments were carried out in airtight flasks over several light-dark cycles. The O_2 levels were monitored in order to derive the rate of O_2 production and consumption. Sampling for Δ_{max} determination was done after the O_2 reservoir was replaced at least five times.
10. The value of Δ_{max} may also be affected by variations in the ratio between normal dark respiration and photorespiration. R. D. Cuy, M. L. Fogel, and J. A. Berry [*Plant Physiol.* **101**, 37 (1993)] determined large but different $^{18}O/^{16}O$ fractionations in these O_2 uptake mechanisms. This may suggest that the $\delta^{17}O/\delta^{18}O$ slope of photorespiration is slightly different than that of dark respi-

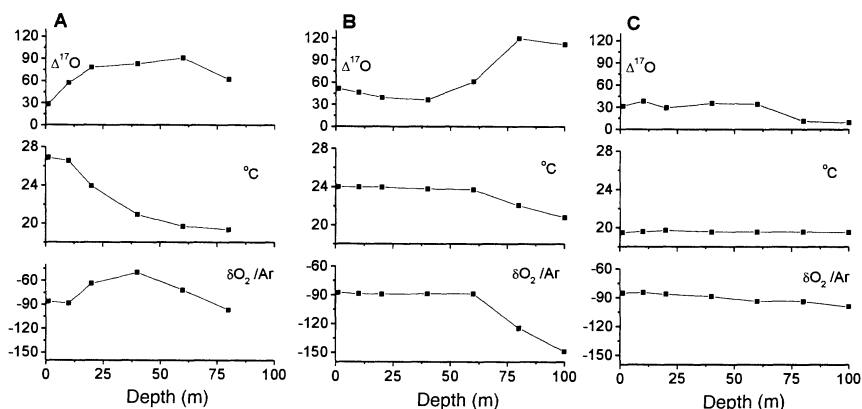


Fig. 2. Depth profiles of $\delta O_2/Ar$ (‰ versus HLA), temperature ($^{\circ}C$), and Δ_{diss} (per meg versus HLA) in BATS Station near Bermuda. (A) Profiles for 7 July 1998. Note the maxima of $\delta O_2/Ar$ and Δ_{diss} in the summer thermocline. (B) Profiles for 7 November 1998. Note the absence of the $\delta O_2/Ar$ maximum. (C) Profiles for 23 March 1999. Note the absence of both maxima.

ration. In this case, variations in the ratio of photo/dark respiration may cause some changes in Δ_{max} , especially in conditions of inorganic carbon limitation favorable to photorespiration such as in terrestrial C_3 vegetation. However, aquatic plants developed mechanisms to concentrate CO_2 and suppress photorespiration [A. Kaplan and L. Reinhold, *Annu. Rev. Plant Physiol. Plant Mol. Biol.* **50**, 539 (1999)]. As a result, photorespiration is not likely to affect oceanic Δ_{max} .

11. H. Craig and L. I. Gordon, in *Conference on Stable Isotopes in Oceanographic Studies and Paleotemperatures*, E. Tongiorgi, Ed. (Laboratory of Geology and Nuclear Science, Pisa, Italy, 1965), pp. 9–130.
12. Air-water equilibrium was attained in less than 24 hours by bubbling outside air into seawater (25°C). The Δ_{eq} value was determined in five separate experiments. Its average value was 16 per meg with a standard error of ± 2 per meg. For simplicity in calculations we assumed that the deviation of Δ_{eq}

from zero is the result of isotopic fractionation occurring only during O_2 invasion. In the cases discussed here, errors due to this assumption are negligible.

13. J. F. Clark *et al.*, in *Air-Water Gas Transfer*, B. Jaehne and E. C. Monahan, Eds. (Aeon Verlag & Studio, Hanau, Germany, 1995), pp. 785–800.
14. P. D. Nightingale *et al.*, *Global Biogeochem. Cycles* **14**, 373 (2000).
15. H. Craig and T. Hayward, *Science* **235**, 199 (1987).
16. W. J. Jenkins and J. C. Goldman, *J. Mar. Res.* **43**, 465 (1985); W. S. Spitzer and W. S. Jenkins, *J. Mar. Res.* **47**, 169 (1989).
17. B. Luz and E. Barkan, data not shown.
18. A. F. Michaels and A. H. Knap, *Deep-Sea Res. II* **43**, 157 (1996); S. C. Doney, D. M. Glover, R. G. Najjar, *Deep-Sea Res. II* **43**, 591 (1996).
19. B. B. Benson and D. Krause Jr., *Limnol. Oceanogr.* **29**, 620 (1984).

20. Data is found at www.bbsr.edu/Weather/dimatology.html; R. Wanninkhof, *J. Geophys. Res.* **97**, 7373 (1992).

21. We are grateful to M. Bender for numerous discussions on all aspects of this research. Comments by A. Kaplan, Y. Kolodny, and three anonymous reviewers significantly improved the manuscript. We appreciate the help of the Bermuda Biological Station in sampling at BATS and extend special thanks to S. Bell. The support of the Kinneret National Laboratory is appreciated. Y. Yacobi and Y. Sagi helped in gross-production measurements in the Sea of Galilee, and J. Erez and K. Schneider helped with the coral experiment. The support of the U.S.-Israel Binational Science Foundation, The Israel Science Foundation, MARS-2, and the Moshe-Shilo Minerva Center is greatly appreciated.

6 December 1999; accepted 11 May 2000

A Low-Operating-Temperature Solid Oxide Fuel Cell in Hydrocarbon-Air Mixtures

Takashi Hibino,^{1*} Atsuko Hashimoto,¹ Takao Inoue,² Jun-ichi Tokuno,² Shin-ichiro Yoshida,² Mitsuru Sano²

The performance of a single-chamber solid oxide fuel cell was studied using a ceria-based solid electrolyte at temperatures below 773 kelvin. Electromotive forces of ~900 millivolts were generated from the cell in a flowing mixture of ethane or propane and air, where the solid electrolyte functioned as a purely ionic conductor. The electrode-reaction resistance was negligibly small in the total internal resistances of the cell. The resulting peak power density reached 403 and 101 milliwatts per square centimeter at 773 and 623 kelvin, respectively.

Fuel cells are widely viewed as a promising source of low-emission power generation for vehicles. There is great controversy over which fuel should be used. Polymer electrolyte fuel cells (PEFCs) exhibit high power densities at low temperatures (~353 K), but they require hydrogen as the fuel, which is impractical in terms of storage and handling. An external reformer can be used to convert alcohols and hydrocarbons into hydrogen, but their portability is inferior. There have been recent successes with solid oxide fuel cells (SOFCs), which perform well between 823 and 973 K using methane (1) and *n*-butane (2) directly as the fuels. A further reduction in the operating temperature of SOFCs and an enhancement in their thermal and mechanical shock resistance would make this technology a promising alternative to PEFCs.

A type of fuel cell that consists of only one gas chamber, where both the anode and the cathode are exposed to the same mixture of fuel and air, has been proposed by many

researchers (3–8). This design is more shock resistant than conventional fuel cells, both thermally and mechanically. We have recently succeeded in applying this single-chamber cell design to a SOFC constructed from yttria-stabilized zirconia (YSZ), which is commonly used as a solid electrolyte in SOFCs, with a Ni-based anode and a perovskite cathode (9). This SOFC, however, must operate at the high temperature of 1223 K to achieve sufficient ionic conduction in the solid electrolyte.

Different cation-doped ceria, notably samaria-doped ceria (SDC), have much higher ionic conduction than YSZ in an oxidizing atmosphere, whereas they show n-type semiconduction in a reducing atmosphere (10, 11). Because the resulting electromotive force (EMF) of the SOFC is lower than the theoretical value, the SDC electrolyte has so far been regarded as unsuitable for such applications. However, the partial pressure of oxygen at the boundary of the two atmospheres becomes gradually lower as the operating temperature decreases (12), which suggests that the SDC electrolyte can be used even under fuel cell conditions, provided it operates at extremely low temperatures. In this report, we demonstrate a low-temperature SOFC by combining the advantages of the SDC electrolyte with the single-chamber cell design.

The SDC electrolyte we used here was prepared by pressing a commercial ceramic powder, $Ce_{0.8}Sm_{0.2}O_{1.9}$ (Anan Kasei Co. Ltd.), hydrostatically into a pellet at $2 \times 10^3 \text{ kg cm}^{-2}$ and then sintering in air at 1773 K for 10 hours. After the pellet was cut into a disk (diameter 14 mm, thickness ~1 mm), the SDC disk surface was polished to a given thickness (0.15 to 0.50 mm) with an abrasive paper. YSZ (8 mol% yttria) and $La_{0.9}Sr_{0.1}Gd_{0.8}Mg_{0.2}O_3$ (LSGM) were used as solid electrolytes for comparison. Preliminary experiments revealed that 10 weight % SDC-containing Ni and $Sm_{0.5}Sr_{0.5}CoO_3$ electrodes best functioned as the anode and the cathode, respectively. These pastes were smeared on the opposite surfaces (area 0.5 cm^2) of the SDC disk, followed by calcining in air at 1223 K for 4 hours. The cell thus fabricated was placed in an alumina tube (inner and outer diameters 15 and 19 mm, respectively). Methane, ethane, and propane were mixed with air for each of the respective concentrations—30 volume % for methane, 18 volume % for ethane, and 14 volume % for propane—so that the oxidation would proceed safely without exploding (the explosive limits of methane, ethane, and propane in air are 15.0, 12.5, and 9.5 volume %, respectively). The gas mixture was supplied to the cell at flow rates of 300 ml min^{-1} between 623 and 773 K (Fig. 1).

When the single-chamber SOFCs using SDC, YSZ, and LSGM with a thickness of 0.50 mm were supplied with a mixture of ethane and air at 773 K, all three cells generated stable EMFs of ~920 mV, where the

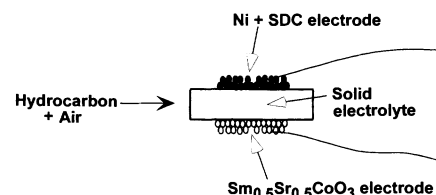


Fig. 1. A schematic illustration of single-chamber SOFC in a flowing mixture of hydrocarbon and air.

¹Department of Structure Formation Process, National Industrial Research Institute of Nagoya, Nagoya 462-8510, Japan. ²Graduate School of Human Information, Nagoya University, Nagoya 466-0804, Japan.

*To whom correspondence should be addressed. E-mail: thibino@nirin.go.jp